Infrared Scanning Near-Field Optical Microscopy (IR-SNOM) Below the Diffraction Limit

J. S. Sanghera, I. D. Aggarwal, A. Cricenti*, R. Generossi*, M. Luce. P. Perfetti*
G. Margoritondo, N. Tolk***, and D. Piston*****

Naval Research Laboratory, Code 5606, Washington, DC, USA
**Instituto di Stuttura della Materia, Rome, Italy*
***Institut de Physique Appliquee, Ecole Polytecnique Federale, Lausanne, Switzerland*
****Vanderbilt University, Nashville, TN, USA*

Abstract: Infrared Scanning Near-field Optical Microscopy (IR-SNOM) is an extremely powerful analytical instrument since it combines IR spectroscopy's high chemical specificity with SNOM's high spatial resolution. In order to do this in the infrared, specialty chalcogenide glass fibers were fabricated and their ends tapered to generate SNOM probes. The fiber tips were installed in a modified near field microscope and both inorganic and biological samples illuminated with the tunable output from a free-electron laser located at Vanderbilt University. Both topographical and IR spectral images were simultaneously recorded with a resolution of ~50 nm and ~100 nm, respectively. Unique spectroscopic features were identified in all samples, with spectral images exhibiting resolutions of up to $\lambda/60$, or at least 30 times better than the diffraction limited lens-based microscopes. We believe that IR-SNOM can provide a very powerful insight into some of the most important bio-medical research topics.

1. Introduction

In the 1870s, Ernst Abbe demonstrated, closely followed by Lord Rayleigh, that, due to diffraction, the lens-based microscopes are limited in their resolution to no better than $\lambda/2n \sin\theta$ (λ being the wavelength of the light used to illuminate the object, n the refractive index of the medium, and θ the aperture half-angle of the optical system) [1-4]. Therefore, the best resolution achievable using visible light with conventional microscopes is around 300 nm. The diffraction limit is even more troublesome with the relatively long wavelengths of the infrared light, limiting the resolution to several microns. Many microscopy techniques (scanning tunneling microscopy (STM), atomic force microscopy (AFM), scanning electron microscopy (SEM), etc.) were developed in order to overcome this limit. Still, none of these microscopy techniques is capable of gathering optical information about the sample. Scanning Near-Field Optical Microscopy (SNOM) is a purely optical microscopy technique, which allows us to form images with resolution well beyond the diffraction limit [3-9]. We will present SNOM images working with infrared light with resolutions of the order of up to $\lambda/60$, which is considerably below the diffraction limit. With our SNOM setup, we routinely get optical resolutions between 50 and 150 nm, regardless of the wavelength of the light

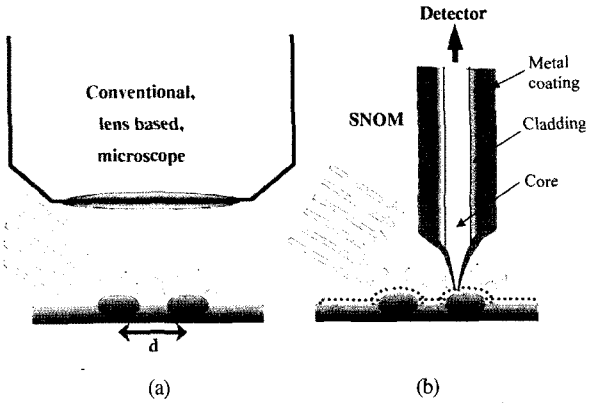

Fig. 1. Comparison between a conventional optical microscope (a) and a SNOM optical fiber tip (b).

used to illuminate the sample[4,10-12].

2. SNOM Fundamentals

With a conventional microscope (Fig. 1(a)), we actually detect a superposition of light coming from every part of the sample under the objective, which means a superposition of diffraction patterns of every shape on the sample. When the distance between the two shapes becomes smaller than $\lambda/2n \sin \theta$ we can not resolve the two objects anymore[1,2]. SNOM collects light through a small aperture at the tip of a tapered optical fiber that is scanned over the sample (Fig. 1(b)). The light is conducted from the sample, through the fiber, to the detector. In our experiments, the sample was illuminated from the outside, as shown on the right side of Fig. 1. During the scanning, the fiber tip is at a constant and a very small distance (of the order of few nanometers) from the sample. The signal is collected only from a very small portion of the sample, approximately the same size as the aperture at the optical fiber tip. The resolution is no longer limited by the diffraction; it depends solely on the size of the aperture of the optical fiber[3-8].

3. Experimental Details

There were important experimental challenges to overcome in order to perform successful spectroscopic IR-SNOM experiments. For example, all the SNOM setups working with visible light use the telecommunications' silica optical fibers. These fibers have strong absorption in the IR spectral region and are therefore unsuitable for IR- SNOM. Working in the infrared enables us to perform spectroscopic characterization and identification based on the fact that practically every molecular species possesses a characteristic vibrational absorption spectrum. We also needed a tunable, monochromatic IR source in order to perform spectroscopic measurements.

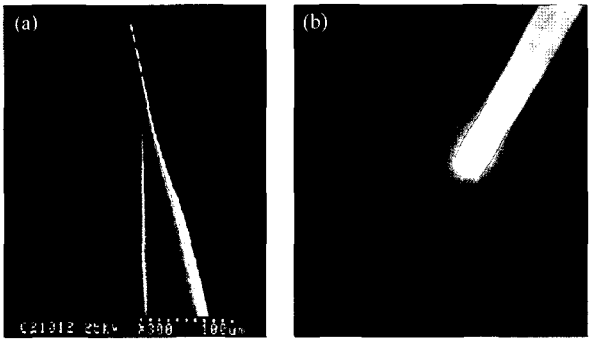

Fig. 2. Tapered ends of the chalcogenide optical fibers made using different techniques, (a) thermal stretching and (b) chemical etching.

The fabrication of extremely high quality infrared fiber tips is a crucial technical step in the practical realization of our experiments. Tapered IR-SNOM probes were obtained from single-mode and multimode, 1m long arsenic selenide or sulfide fibers using both thermal stretching and a chemical etching process (Fig. 2) [4,15-17]. Fiber tips made by thermal pulling of the fibers did work but are less reproducible than etching due to relatively tight constraints on the temperature gradients. A SMA adapter was then fitted on one fiber end using phenyl salicylate as support to keep the fiber firmly in place. This was done by melting the phenyl salicylate with a hot plate and applying the liquid state to the adapter opening while holding the fiber in place. Likewise, phenyl salicylate was applied around the fiber projecting from the SMA. This fiber end was polished down using water as a lubricant to a smooth clean surface with 12-, 3-, and 0.3-μm polishing discs (Buehler). The endface was then checked with a microscope to examine the effectiveness of the polishing. The other end was chemically etched into a fiber tip using a protective layer etching system[15]. At room temperature, the arsenic sulfide tip was etched with KOH and the arsenic selenide tip was etched using a piranha solution (7:3, H_2O_2:H_2SO_4). The time-to-completion for the etching process depended on etchant concentration, temperature, and fiber diameter, and typically ranges from 15 min to 1 h. An optical microscope was used to monitor the etching progress. The etched tips were coated with aluminum or gold (both worked equally well) using a Varian thermal deposition system at a pressure of 10^{-6} Torr with the tips at a 25°-30° angle above the evaporation point source to create an aperture. The tips are rotated to achieve a uniform coating with a thickness of approximately 100 nm [4,15-17].

Another key technical problem in IR spectroscopic SNOM is the need for the IR source to be tunable over a broad band and intense enough to offset the limited sub-wavelength aperture transmission. The Vanderbilt

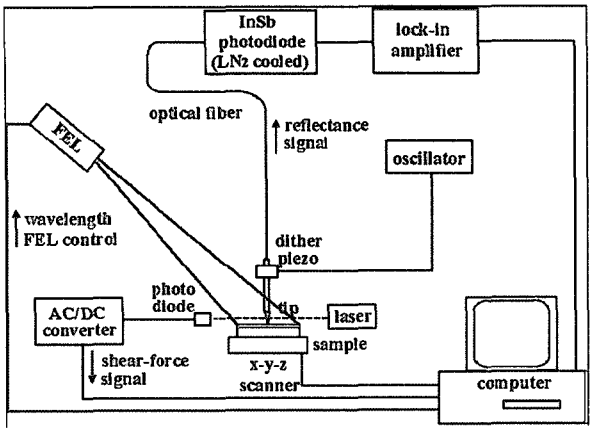

Fig. 3. Schematic diagram of our experimental set-up.

University free electron laser (FEL) is continuously tunable over a broad wavelength range (2.1-9.8 μm) and is intense and stable, therefore, ideal for IR spectroscopic SNOM. While the use of a free electron laser source limits applications to the relatively few researchers who can access such a device, in principle the general technique could be applied to alternative tunable IR laser sources. For example, the availability of rare earth doped chalcogenide glass fiber laser sources would enable compact sources for IR-SNOM. The near field microscope rested on an optical bench as part of an optical network where the laser beam could be transmitted and focused onto the sample stage of the microscope (Fig. 3). A fiber tip was then installed into the microscope with the output end lens-coupled to a liquid nitrogen-cooled indium antimonide infrared detector. The FEL beam illuminates the specimen over a broad area (~1mm spot diameter) and the SNOM probe collects the reflected light. Reflectivity images and topography images were simultaneously obtained while scanning over the sample while illuminated by the infrared FEL light. Scanning of the sample took place over an area ranging from 1×1 μm to about 20×20 μm. Relative to the scanning area, the 1-mm diameter spot size of the FEL beam was broad and insured good sample illumination. The average energy level of the FEL was approximately 30 mJ/macropulse (4-5 ms pulse-width) at a 30-Hz frequency. Reflectivity was collected using a standard lock-in technique. Topography images were obtained by measuring the shear force signal by synchronous detection using a piezoelectric oscillator and AC/DC converter. We use the shear force feedback mechanism to control the tip-to-surface distance. Resonant lateral ($x-y$ plane) oscillation of the fiber is induced. The sulfide tip's mechanical resonant frequency was approximately 11 kHz whereas the selenide tip resonated at a lower frequency of 8.5 kHz. This difference is mostly due to differences in their stiffness/modulus. When the fiber's tip is at a few nanometers from the sample, the amplitude of the oscillation starts to be damped by shear forces (typically Van der Waals forces). The amplitude is monitored and fed into a feedback loop, which then moves the tip in the z direction (towards and from the sample) in order to always have a constant damped amplitude of the oscillation (typically, we get the best results with 10-20% damping).

4. Results and Discussion

4.1 Polycrystalline Diamond Films

Our first tests of IR spectroscopic SNOM were performed on synthetic polycrystalline diamond films grown by plasma-assisted chemical vapor deposition (CVD)[16]. In principle, these films should be hydrogen-free after annealing to remove residual hydrogen and water. However, FTIR spectroscopy showed the presence of hydrogen (Fig. 4, top). We tested this point by tuning the FEL to a wavelength 3.5 μm, corresponding to a C−H vibrational stretch mode absorption band. Fig. 4 (bottom, left-hand side) shows three 10×10 μm SNOM reflectivity images obtained at a wavelength of 3.5 μm and with two off-absorption wavelengths. On these images, darker areas correspond to lower light intensity collected by the SNOM fiber tip. Contrary to the on-absorption image, the two off-absorption images are featureless. The comparison with the corresponding shear-force (topological) image, on the bottom right-hand side of Fig. 4 can be used to assess the possible presence of artifacts. The dark regions of the on-absorption SNOM image indicate the presence of residual hydrogen mainly around grain boundaries. For the topographic images, line scans yield resolution estimates between 50 and 80 nm, demonstrating the high quality of the fiber tips. Similar line scans for the spectroscopic SNOM images demonstrate a lateral resolution of 200 nm, well beyond the diffrac-

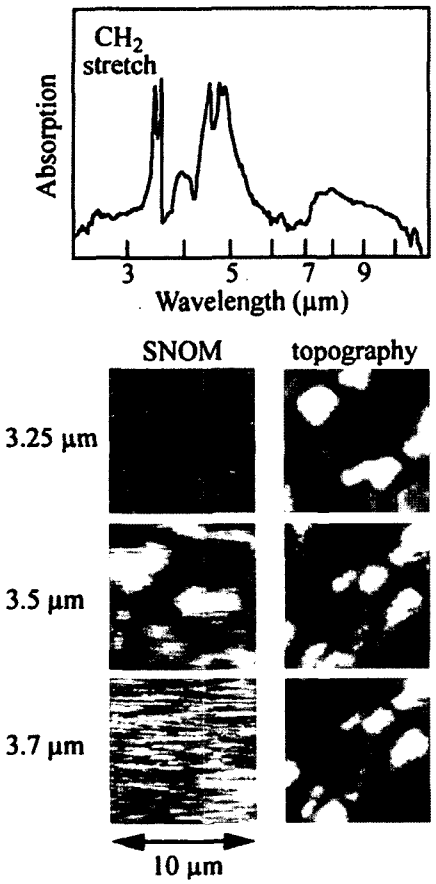

Fig. 4. Results for polycrystalline diamond films grown by plasma-assisted chemical vapor deposition (CVD). Top: absorption spectrum. Bottom: spectroscopic (reflectivity) SNOM images and shear-force topographic images taken with three different wavelengths. The 3.5 μm wavelength corresponds to a C-H vibrational stretch mode absorption band and reveals the presence of hydrogen.

tion limit. This was the first successful test of IR spectroscopic SNOM and confirmed the FTIR results showing that hydrogen was in fact present in this nominally hydrogen-free system. The SNOM test provided information on the hydrogen distribution and opened the door to spectroscopic SNOM tests in other systems.

4.2 Boron Nitride Films Results

Cubic boron nitride (c-BN) films have physical and chemical properties very similar to those of diamond: extreme hardness, excellent chemical inertness, thermal stability and wide band gap. Cubic boron nitride is superior to diamond in some aspects. For example, diamond is readily oxidized at elevated temperature while c-BN

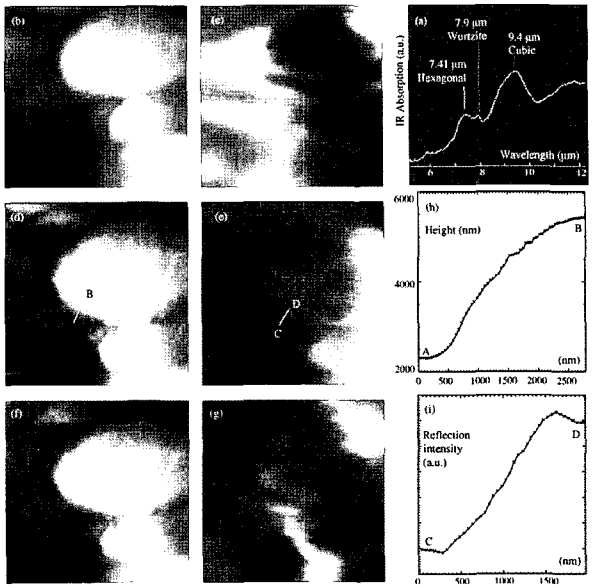

Fig. 5. BN results: (a) FT-IR spectrum with the vibrational modes corresponding to three crystallographic phases; (c), (e) and (g) are spectroscopic (reflectivity) SNOM images at the wavelengths 9.4, 7.9 and 7.41 μm; (b), (d) and (f) are corresponding topographic images; (h) is a topography cross-section corresponding to the line A-B in (d) and (g) is an intensity profile for the line C-D in (e).

is not. Recently, this stimulated an important research on synthesis of high quality c-BN films. However, the growth of c-BN is difficult: the typical crystal phase of BN films is a mixture of the cubic and of the hexagonal (h-BN) phase[17], which is less attractive for industrial use. In our experiments, BN films are grown on silicon wafers by laser induced chemical vapor deposition (LCVD). Undesired hexagonal and wurtzite crystal phases are always present in the films. Our experiment targets different vibration modes corresponding to these different crystallographic phases present in the BN film. The FTIR spectrum of Fig. 5(a) reveals several vibration modes. Of these, the features at 9.4, 7.9 and 7.4 μm are associated respectively to the cubic, wurtzite and hexagonal BN crystal phases. The spectroscopic (reflectivity) SNOM images of Fig. 5(c) (acquired with FEL illuminating the sample with λ = 9.42 μm, strongly absorbed by c-BN), Fig. 5(e) (acquired with FEL illuminating the sample with λ = 7.94 μm, strongly absorbed by w-BN) and Fig. 5(g) (acquired with FEL illuminating the sample with λ = 7.41 μm, strongly absorbed by h-BN) clearly reveal

differences in the lateral distribution of such phases. Darker color on these images indicates more absorption. Fig. 5(b, d) and (f) are, respectively, topographic images corresponding to Fig. 5(c, e) and (g). They show that the three scans have been performed over the same part of the sample. The strongest absorption from the cubic phase (Fig. 5(c)) arises from the three large grains that can be seen on the right side of the topographic images. In contrast, the wurtzite phase (Fig. 5(e)) is mainly present on the left side of the image, in the lower parts of the sample, closer to the substrate. A weak hexagonal contribution (Fig. 5(g)) seems to be coming from all over the sample. The lower intensity of the signal can be explained if we suppose that the hexagonal phase is actually on the interface with the substrate, under the layer of the c-BN. Our results confirm similar observations reported with other experimental techniques[17]. However, SNOM offers several advantages over the experimental technique used in[17]: it is completely non-destructive and provides additional information, such as the size of the grains. Fig. 5(i) shows a reflected signal cross-section along the line C – D in Fig. 5(e). This cross-section shows clearly that we achieved a resolution of better than 1 μm, while the illumination wavelength was $\lambda = 7.94$ μm. So, we have achieved a resolution at least four times better than the one imposed by the diffraction limit and accessible to the lens-based microscopes. Cell results shown in this article demonstrate that the actual resolution of our SNOM is even higher, but in these BN samples the distribution of different phases does not allow sharper optical contrast.

4.3 Semiconductor Material

The sample scanned was an integrated micro-circuit i.e., semiconductor material. Fig. 6 shows the corresponding topography and reflectivity images obtained at a wavelength of 4.7 μm for a 1×1 μm area on the integrated circuit. The topography shows a flat surface on the order of a few nanometers while the corresponding optical image indicates a 100 nm wide dark region that is caused by a reflectivity change in a topographically smooth area. The data suggests that a subsurface defect or a small material heterogeneity may reside at this specific location which produces a band at 4.7 μm. This detected change in signal could be a

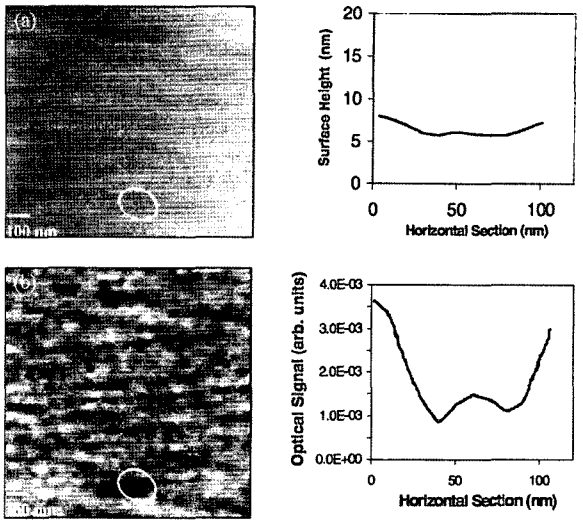

Fig. 6. (a) Topographical image using a selenide tip. The cross section taken in the circled area is very smooth and featureless in the topography. (b) Corresponding optical image at 4.7 μm. There is a significant localized change (100 nm) in the optical image indicating a heterogeneity.

change in reflectivity caused by a refractive index change and/or absorption change in the material due to unique chemical vibrational modes.

4.4 LiF Crystals

LiF films are quite interesting as potential components of miniaturized optical devices. The creation of defects, called "color centers" [18] can lead to the stable formation of active, visible emitting electronic defects. Such defects can be created by different processes; in the present case, we explored the results of an innovative irradiation technique[19] based on extreme ultraviolet (EUV) radiation and soft X-rays emitted by a laser plasma-point source. This approach can produce patterned coloration on large areas.

High-quality LiF films were grown by thermal evaporation on untreated silicon substrates at 250°C. The films total thickness, measured by a stylus profilometer after the growth, was about 800 nm. EUV and soft X-ray radiation was produced by focusing an excimer laser beam (wavelength = 308 nm) on a tape shaped solid target in vacuum. The LiF was also in vacuum ~12 cm from the plasma source; the irradiated area was several square centimeters. A colored pattern was obtained by placing on the LiF films a copper mesh (wire diameter 10 μm, period 12.7 μm). Fig. 7(a) shows

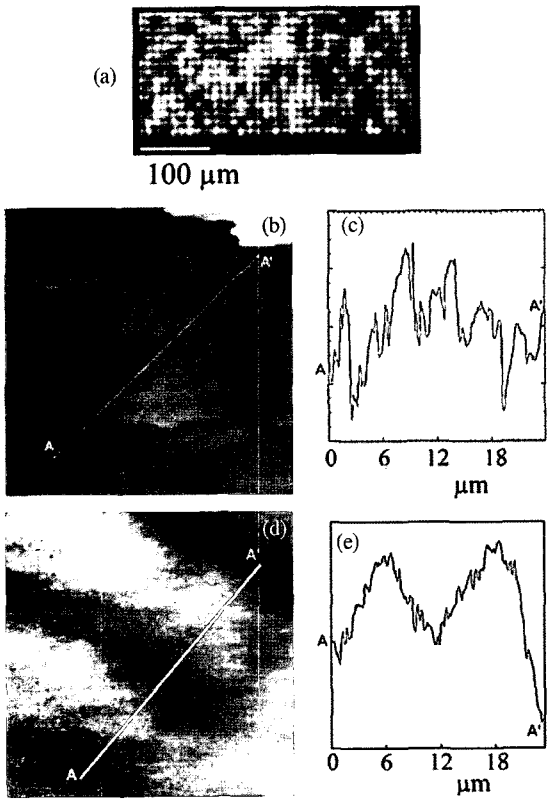

Fig. 7. *Results on a LiF film on silicon with patterned coloring by X-ray irradiation.* (a) fluorescence optical micrograph of the colored pattern (the white spots correspond to irradiated areas). (b) 20x20 μm shear-force image. (c) Intensity profile along the marked line of Fig. 7(b). (d) Spectroscopic (reflectivity) SNOM image taken with a wavelength of 6.1 μm. (e) Intensity profile along the marked line of Fig. 7(d).

a fluorescence optical micrograph of the colored pattern; the white spots correspond to irradiated areas. Fig. 7(b) is a 20×20 μm shear force image showing LiF surface topography (the corresponding profile is in Fig. 7(c)). Fig. 7(d) shows the corresponding spectroscopic (reflectivity) SNOM image taken with a wavelength of 6.1 μm. At this wavelength we can clearly observe contrast in the image that is not correlated to the topographic SNOM features, and shows a periodicity corresponding to the pattern shown in Fig. 7(a). Similar results were obtained with images taken at a wavelength of 9.2 μm. Thus, the search for irradiation-induced lateral fluctuations in the refractive index was successful. Since there is no special absorption in this spectral region we ascribe the change in reflectivity to be due to a variation of the refractive index of the exposed LiF material. Fig. 7(e) shows an intensity profile along the marked line of Fig. 7(d). From such profiles, we estimated a lateral resolution of 200-300 nm (50 nm in the topographic images), again much better than the diffraction limit corresponding to the 6.1 and 9.2 μm wavelengths[20].

4.5 Biological Growth Medium

These experiments were performed on a thick silicon substrate that was submersed in a postgate growth medium solution at room temperature for one month. In preparation for our near field experiments, the silicon substrate was removed from the medium solution,

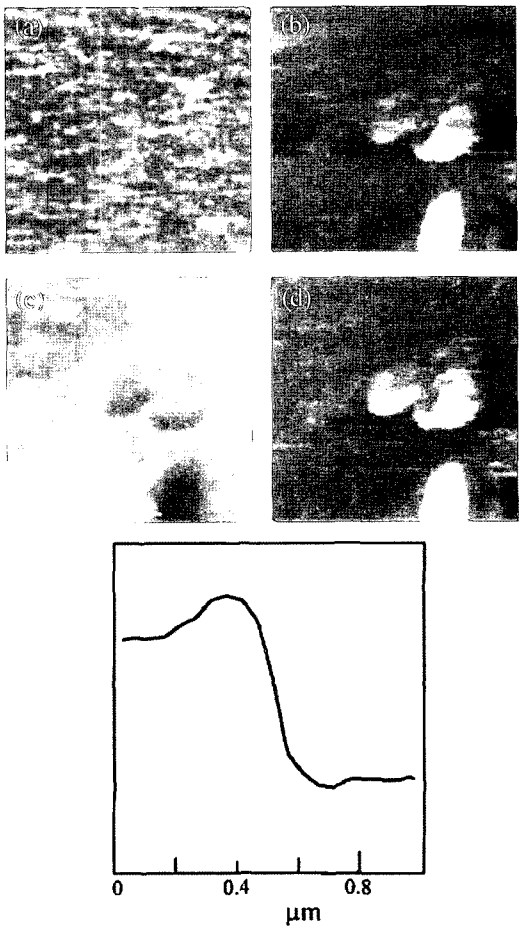

Fig. 8. Results on a thin films of a biofilm growth medium. (a) 20×20 μm SNOM reflection images obtained with λ= 6.6 μm, and (b) the corresponding topographic image. (c, d) Equivalent images for λ=6.95 μm corresponding to the vibrational stretch mode absorption bands of sulfur and nitrogen compounds. Darker areas correspond to stronger absorption. (e) Intensity profile taken along the marked line of Fig. 8(c).

dipped in deionized water, and allowed to dry before observing the next day. Once dry, areas of film deposition residing on the silicon surface were observed using an optical microscope, and subsequently observed with the near field microscope[21]. The growth medium is composed of several products[22], primarily sulfur and nitrogen-oxide compounds, whose vibrational stretch mode absorption bands occur in the infrared around 7 μm[23]. IR Spectroscopic (reflectivity) SNOM images were taken at wavelengths of 6.95 and 6.6 μm, inside and outside the absorption region. Fig. 8 shows 20× 20 μm spectroscopic SNOM images together with the corresponding shear force topography images. The topological images show the presence of several biological growth medium grains with width and height of a few micrometers. The contrast between the featureless off-absorption (6.6 μm) image and the rich microstructure in the on-absorption (λ = 6.95 μm) image is quite striking. Line scans like that of Fig. 8e reveal a resolution of 200 nm for the spectroscopic images and about 50-80 nm for the topographic images. A lateral resolution value better than λ/30 was obtained at 6.95 μm.

4.6 Keratinocyte Cells (HaCaT cell line)

We recorded SNOM images of keratinocyte cells (HaCaT cell line). The cells were seeded on glass cover slides; after 24 h the growth medium was removed and the cells were fixed in paraformaldehyde and washed twice with phosphate-buffered saline (PBS) and twice with distilled water. We performed the test scans by targeting IR absorptions of several chemical bonds and cell constituents. We used the FEL to illuminate the sample at different wavelengths: Fig. 9(d): λ = 6.1 μm, targeting the so called amide I absorption band, corresponding to the CO bond stretch absorption. The CO bond is present in all the proteins, at every link between two amino-acids; Fig. 9(c): λ = 6.95 μm, a wavelength strongly absorbed by the sulfide stretch band, mainly from the cell growth medium; Fig. 9(b): λ = 8.05 μm, strongly absorbed by the phosphorus stretch band, mainly concentrated in the DNA and the RNA. Fig. 9(a) shows the corresponding topography. Darker color in Fig. 9d indicates the position of proteins. Proteins are quite homogeneously distributed in cells and, as expected, there is a steady absorption arising from all over the cell. The cross-section (Fig. 9(e)) of the reflected signal

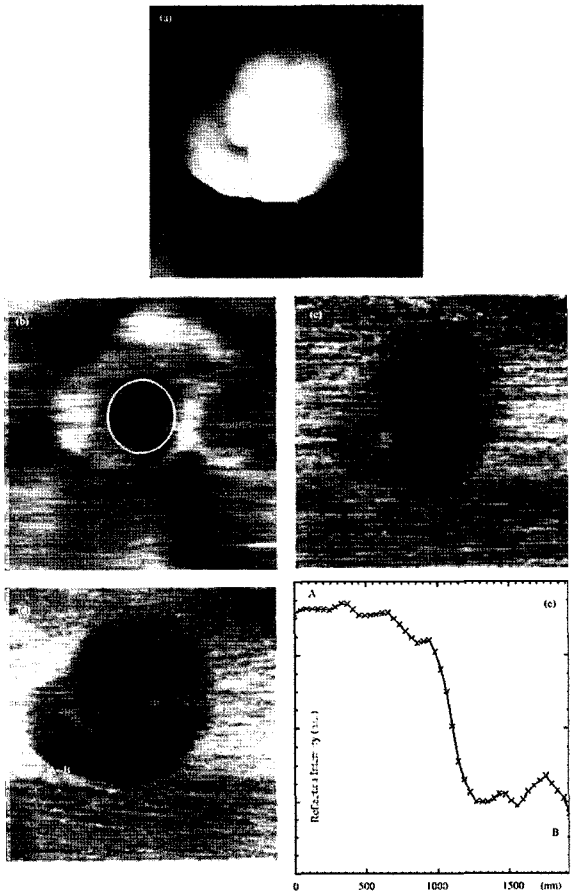

Fig. 9. Keratinocyte cell (HaCaT cell line) SNOM images: (a) shows the topography; (b), (c) and (d) are reflectivity SNOM images at the wavelengths 8.05, 6.95 and 6.1 μm, respectively; (e) shows a profile of the reflected intensity along the line A–B (in (d)), demonstrating the resolution of the order of 100 nm (or λ/60, 30 times superior to the resolution of the conventional lens-based microscopes).

along the line A–B (Fig. 9(d)) allows us to asses the resolution of our setup: it is of the order of 100 nm, or λ/60. This is at least 30 times better than the diffraction limited lens-based microscopes. Fig. 9(c) also shows a steady absorption from all over the cell, indicating that even washed, our cells still contain important amounts of the cell growth medium, while the coverslip substrate does not. Fig. 9(b) shows important absorption only on one part of the cell (within the white circle in the Fig.). This is due to the localization of the DNA inside the nucleus, which yields a strong local absorption seen in the SNOM image. FTIR measurements show only a relatively low absorption at this wave-

length. Such absorption has been seen with FTIR only on cells during replication, possibly because of the spatial extension increase of the nucleus[24].

4.7 Pancreatic Cells

Rat pancreatic b-cell line (INS-1 cells) were seeded on glass cover slides[25]. After 24 h the medium was removed and the cells were fixed in paraformaldehyde and washed twice with phosphate-buffered saline (PBS). Since these cells were fixed, we could rinse them with pure water and dry them before SNOM imaging. Once again, the shear-force topography images were independent of the wavelength (Fig. 10(a, c) and e) and the SNOM images dramatically different for different wavelengths. The images for $\lambda = 6.1$ μm (amide I, CO stretch band; Fig. 10(b)) and $\lambda = 6.95$ μm (sulfide stretch band; Fig. 10(f)) show absorption within the cell, as opposed to the $\lambda = 6.45$ μm image (Fig. 10(d)), which shows much less contrast. Although we would expect absorption in the cell at both the amide I band (6.1 μm) and the amide II band (6.45 μm), the contrast mechanism in the images is not solely governed by the cellular properties, but also by the properties of the background. This can be seen in Fig. 10(b) and f, where the reflected signal outside the cell is larger than it is in Fig. 10(d). Thus, the contrast at 6.1 μm and 6.95 μm is larger than it is for 6.45 μm.

We also performed experiments at several different wavelengths on COS-7 cells that had not been fixed[25]. The cells were dried in buffer and imaged immediately with just a thin coating of aqueous buffer. As shown in Fig. 11(a), cells could be detected by shear-force topography, but crystals of the PBS were also clearly observed. The topographic images were once again λ-independent. The SNOM images, however, were seen to be strongly dependent on the wavelength. In particular, the 8.05 μm image (Fig. 11(b)) corresponding to the phosphate stretch band shows the PBS crystal as an extremely dark object, and also reveals absorption in the region of the cell nucleus. Differences in absorption are visible between the cell and the crystal: for example, only the crystal reflects at 7.6 μm (Fig. 11(c)). In the case of the COS-7 cells, the strongest absorption is at 8.05 μm, corresponding to the phosphate region associated with RNA and DNA. This result may be due to the localization of the DNA nuclei, which yields

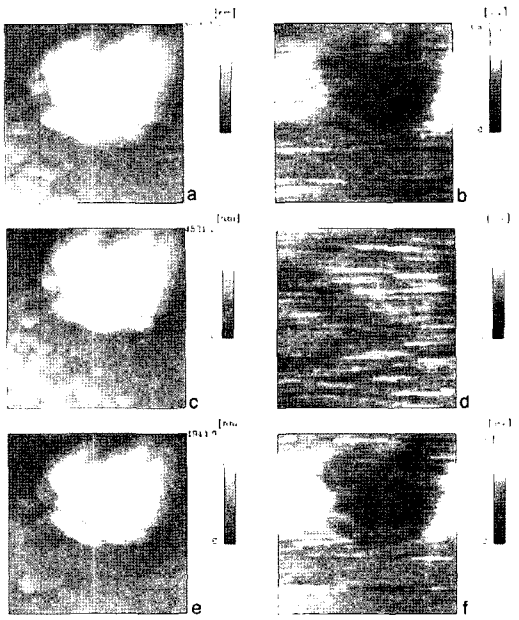

Fig. 10. Several 20x20 μm SNOM reflection images of tissue culture cells from a rat pancreatic b cell line (INS-1) in liquid. (a, b) topographic image and spectroscopic (reflectivity) image at a wavelength of 6.1 μm; (c,d) similar images for 6.45 μm; (e,f) similar images for 6.95 μm.

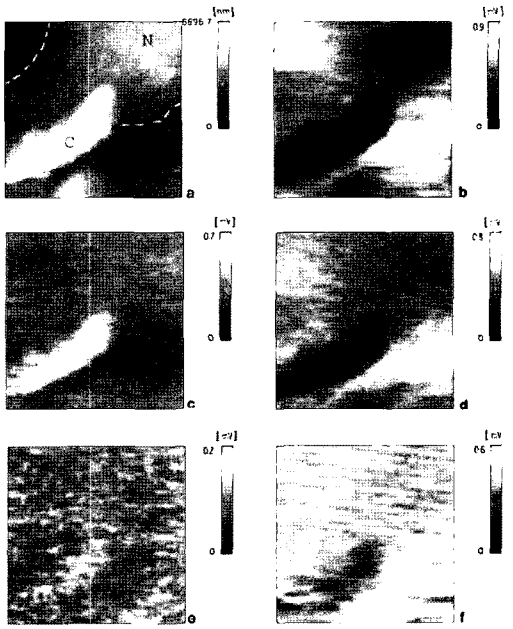

Fig. 11. (a) 20x20 μm shear-force (topographic) image of a COS-7 cell in PBS. The cell body and nucleus (upper right) are seen and a crystal of PBS (left side) can also be seen on the cell. SNOM reflection images of the same field were obtained under illumination with (b) λ= 8.05 μm, (c) λ=7.6 μm, (d) λ=6.95 μm, (e) λ=6.45 μm, and (f) λ=6.1 μm. PBS crystal is labeled "C", and the cell nucleus is labeled "N".

a strong local absorption seen in the SNOM image, but a relatively low absorption in the FTIR measurements. Such absorption has been seen in FTIR, for example, in cells during replication, possibly because of the spatial extension increase of the nucleus. By using SNOM, it is possible to reveal a more accurate estimation of the chemical composition due to the small field of view given by the high resolution (small tip aperture). In this case, the dense-packed nucleus can be easily detected because of the relative increase in absorption compared to the background. As we have characterized, for the first time, wet cells, we emphasize that no insurmountable obstacles exist that would disallow the use of this approach for live cellular systems. Similar measurements will be possible on samples submerged in water by using both illumination and detection through the same fiber.

4.8 Magnetic Field Effect on Cells

Are low-frequency electromagnetic fields capable of modifying human cells? Even though several studies indicate that the biochemical parameters can indeed be significantly affected[26-32] this question remains controversial. Consequently, we used IR-SNOM to detect chemical modifications induced by exposure to an electromagnetic field. We focused our attention on one potential type of magnetic field effect: intracellular biochemical reactions that involve more than one unpaired electron. Most enzymes do not involve radical intermediates and should not be affected by exposure to magnetic fields. Moreover, for a set of more than 50 enzymes, believed to generate free radical intermediates during catalysis, modifications of activity can, in principle, be caused by magnetic field interactions. However, how can an applied magnetic field strength weaker than typical hyperfine interactions influence the yields and kinetics of recombination reactions of free radicals in solution (the so-called "low field effect")? A plausible mechanism is coherent superpositions of degenerate electron-nuclear spin states. A weak applied magnetic field could cause these states to oscillate, leading to coherent interconversion of singlet and triplet electronic states of the radical pair. This, in turn, would change the yields of recombination products and of free radicals escaping into solution. For singlet geminate radical pairs, this boosts the concentration of free radicals — an effect that could lead to significant biological effects of electromagnetic fields on living systems. To study such phenomena with IR-SNOM, we specifically targeted the spontaneously immortalized human keratinocytes cell line, HaCaT, derived from adult skin[33]. Indeed, the more external part of the skin, the epidermis, is primarily made up of keratinocytes that are the main cells to be affected by external agents such as extremely low-frequency (ELF) magnetic fields. Such cells maintain full epidermal differentiation capacity[34] after 24 h exposure to a 1 mT, 50 Hz magnetic field. The effects of the same exposure with visible fluorescence SNOM and atomic force microscopy (AFM) has been previously explored. Those results revealed modifications in the morphology with an increase of the adhesion areas between cells and a corresponding upsurge segregation of the sulphur rich protein adhesion marker β4 integrin in the cell membrane[35]. The results of Ref. 35 opened the question of significant biochemical variations accompanying the observed morphological changes. We addressed this issue with the present IR-SNOM experiment, obtaining a positive answer. HaCaT cells were grown in D-Mem (GIBCO Laboratories, Scotland) supplemented with 10% Fetal calf serum[36,37] and antibiotics (110 IU/ml of penicillin and 100 μg/ml of streptomycin) at 37±0.3 °C, 5% CO_2, and sub-cultivated twice a week at a 1:5 ratio. Control (unexposed) cells and magnetic field exposed cells used for each of the experiments originated from the same flasks and generation. HaCaT cells were cultured in a complete medium starting at a concentration of 5×10^5 ml^{-1} both for the control and exposed samples. The cells were exposed for 24 h to a sinusoidal magnetic field [50 Hz, flux density of 1 mT (rms)] in a temperature-regulated solenoid. The solenoid was put in a cell incubator whereas control cells were kept in a second incubator of the same type, under the same conditions except for field exposure. As a double check, in a random test the control sample was placed in the cell incubator containing the solenoid with no field, in the same conditions of the exposed cells except for the absence of the field. No differences were detected between the control cells and these "sham" cells. All experiments were performed under blind conditions. Long exposure to temperatures higher than the physiological temperature would of course induce the syn-

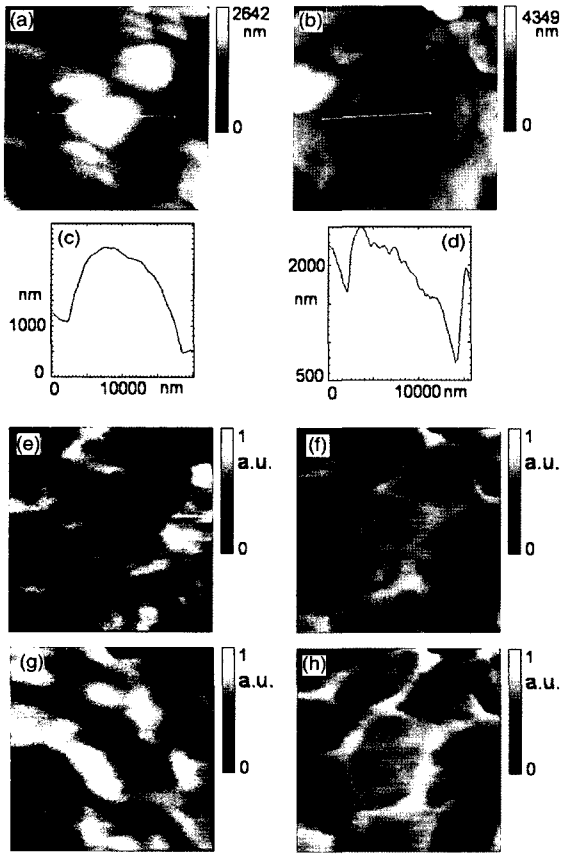

Fig. 12. (a) and (b) Shear-force topography images; (c) and (d) corresponding A-B line profiles; (e) and (f) IR-SNOM optical reflectivity images taken at a wavelength of 6.1 μm; (g) and (h) IR-SNOM optical reflectivity images taken at a wavelength of 6.45 μm. Images (a), (e), and (g) were taken on control (unexposed) HaCaT cells; images (b), (f), and (h) correspond to cells exposed for 24 h to a 50 Hz, 1 mT magnetic field. All image sizes are 30x30 μm.

thesis of heat shock proteins (HSPs). However, western blotting analysis of control cells and exposed HaCaT cells did not reveal any difference in the expression of the heat shock protein HSP-70, indicating no heat stress of the cells. Note an often overlooked fact: inside a solenoid, there exists an almost homogeneous electric field parallel to the magnetic field unless adequate electric shielding is used. An approximate estimate of the electric field induced by capacity coupling in the culture medium was estimated to be very weak, of the order of 0.01 μV/cm.

Fig. 12 shows 30×30 μm topography images (a) and (b) and the corresponding IR-SNOM optical images of unexposed [(e) and (g)] and 24 h exposed [(f) and (h)] HaCaT cells for the 6.1 μm [(e) and (f)] and 6.45 μm [(g) and (h)] wavelengths. These images are representative of a large body of coherent results. The shear-force topography images do not change when the wavelength is modified, whereas the SNOM images do: this is due to the fact that the different components are differently distributed inside the cells. A direct comparison of the optical images for exposed and unexposed cells clearly reveals changes in the spatial distribution of the three cell components. In fact, the optical signals at 6.1 and 6.45 μm in exposed samples are distributed in the overall cell body as compared to the non-exposed ones where we have absorption in limited areas of the cells. This conclusion is clear from visual inspection and corroborated by standard image analysis. This is also in agreement with fluorescence SNOM results on these HaCaT cells, after the same magnetic field exposure, that indicated an increase of segregation in the cell membrane of the protein adhesion marker β4 integrin[37]. Furthermore, the existence of field-induced changes is specifically true for the lipid distribution. The phospholipid organization in a plasma membrane can be affected by the membrane protein structure and composition: it can be interpreted as a reorganization of the phospholipid moiety in the plasma membrane of the exposed cells, due to an increase in the synthesis of the adhesion membrane protein integrin. Also the signals from nucleic acids at 8.05 μm (data not shown) in exposed samples are not only confined to the cell nucleus but distributed in the entire cell body. Independent of the interpretation, the above results clearly reveal significant chemical modifications induced by the low-frequency magnetic field. The topographic images fully confirm the existence of morphological changes, consistent with our previous AFM results for equivalent cells and exposures[34]. Fig.s 12 (c) and (d) show examples of topographic profiles (white lines) of control and exposed HaCaT cells. Whereas the unexposed cell exhibits a round shape, after exposure the cell appears flattened. We determined an experimental resolution of ~80 nm for the topographic images and of ~100 nm for the spectroscopic IR-SNOM images. Overall, we tested three different specimens and analyzed 30 exposed cells and their control counterparts. We found magnetic-field-induced modifications of the type illustrated by Fig. 12 in 85% of the examined cells.

By comparing different control-cell images, we see shape fluctuations that could simulate magnetic-field-induced changes in less than 10% of the cell population. The basic message of our experiments is quite clear: HaCaT cells are significantly affected by ELF magnetic field. Not only did our result confirm morphological changes but they also revealed biochemical variation, brought to light by the distribution of functional groups.

5. Conclusions

Infrared Scanning Near-field Optical Microscopy (IR-SNOM) is an extremely powerful analytical instrument since it combines IR spectroscopy' s high chemical specificity with SNOM' s high spatial resolution. In order to do this in the infrared, specialty chalcogenide glass fibers were fabricated and their ends tapered to generate SNOM probes. The fiber tips were installed in a modified near field microscope and both inorganic and biological samples illuminated with the tunable output from a free-electron laser located at Vanderbilt University. Both topographical and IR spectral images were simultaneously recorded with a resolution of ~50 nm and ~100 nm, respectively. Unique spectroscopic features were identified in all samples, with spectral images exhibiting resolutions of up to $\lambda/60$, or at least 30 times better than the diffraction limited lens-based microscopes. We believe that IR-SNOM can provide a very powerful insight into some of the most important bio-medical research topics.

Acknowledgements

The authors would like to acknowledge the efforts of David Talley, Peter Thielen, Dave Schaafsma, Vinh Nguyen and Pablo Pureza during their work in this area at NRL.

References

1. J.A. O'Keefe, J. Opt. Soc. Am. 46 (1956) 359.
2. M. Born, E. Wolf, Principles of Optics, 6th ed., Pergamon Press, Oxford, 1987.
3. E.A. Ash, G. Nichols, Nature 237 (1972) 510.
4. D. Vobornik, G. Margaritondo, J.S. Sanghera, P. Thielen, I.D. Aggarwal, B. Ivanov, J.K. Miller, R. Haglund, N.H. Tolk, A. Congiu-Castellano, M.A. Rizzo, D.W. Piston, F. Somma, G. Baldacchini, F. Bonfigli, T. Marolo, F. Flora, R.M. Montereali, A. Faenov, T. Pikuz, G. Longo, V. Mussi, R. Generosi, M. Luce, P. Perfetti, A. Cricenti, Infrared Phys. Technol. 45 (2004) 409.
5. D.W. Pohl, W. Denk, M. Lanz, Appl. Phys. Lett. 44 (1984) 651.
6. E. Betzig, J.K. Trautman, Science 257 (1992) 189.
7. E. Betzig, P.L. Finn, J.S. Wiener, Appl. Phys. Lett. 60 (1994) 2484.
8. H. Heinzelmann, D.W. Pohl, Appl. Phys. A 59 (1994) 89.
9. D.W. Pohl, D. Courjon (Eds.), NATO ASI Series "Near-Field Optics", vol. 262, Kluwer Academic Press, 1992.
10. A. Cricenti, R. Generosi, M. Luce, P. Perfetti, G. Margaritondo, D. Talley, J.S. Sanghera, I.D. Aggarwal, N.H. Tolk, A. Congiu-Castellano, M.A. Rizzo, D.W. Piston, Biophys. J. 85 (2003) 2705.
11. A. Cricenti, V. Marocchi, R. Generosi, M. Luce, P. Perfetti, D. Vobornik, G. Margaritondo, D. Talley, P. Thielen, J.S. Sanghera, I.D. Aggarwal, J.K. Miller, N.H. Tolk, D.W. Piston, J. Alloys Compd. 362 (2004) 21.
12. A. Cricenti, G. Longo, M. Luce, R. Generosi, P. Perfetti, D. Vobornik, G. Margaritondo, P. Thielen, J.S. Sanghera, I.D. Aggarwal, J.K. Miller, N.H. Tolk, D.W. Piston, F. Cattaruzza, A. Flamini, T. Prosperi, A. Mezzi, Surf. Sci. 544 (2003) 51.
13. D.B. Talley, L.B. Shaw, J.S. Sanghera, I.D. Aggarwal, A. Cricenti, R. Generosi, M. Luce, G. Margaritondo, J.M. Gilligan, N.H. Tolk, Mater. Lett. 42 (2000) 339.
14. D.T. Schaafsma, Opt. Eng. 38 (1999) 1381.
15. D.T. Schaafsma, R. Mossadegh, J.S. Sanghera, I.D. Aggarwal, J.M.Gilligan, N.H. Tolk, M. Luce, R. Generosi, P. Perfetti, A. Cricenti, G. Margaritondo, Ultramicroscopy 77 (1999) 77.
16. A. Cricenti, R. Generosi, M. Luce, P. Perfetti, G. Margaritondo, D. Talley, J.S. Sanghera, I.D. Aggarwal, J.M. Gilligan, N.H. Tolk, J. Microsc. (Oxford) 202 (2001) 446.
17. J. Tian, L. Xia, X. Ma, Y. Sun, E.-s. Byon, S.-h. Lee, S.-r. Lee, Thin
18. Solid Films 355-356 (1999) 229. U.M. Grassano, G. Margaritondo, R. Rosei, Phys. Rev. B2 (1970) 3319.
19. G. Baldacchini, F. Bonfigli, F. Flora, R.M. Monatereali, D. Murra, E. Nichelatti, A. Faenov, T. Pikuz, Appl. Phys. Lett. 80 (2002) 4810.
20. A. Cricenti, G. Longo, V. Mussi, R. Generosi, M.

Luce, P. Perfetti, D. Vobornik, G. Margaritondo, P. Thielen, J. S. Sanghera, I. D. Aggarwal, N. H. Tolk, G. Baldacchini, F. Bonfigli, F. Flora, T. Marolo, R.M. Montereali, A. Faenov, T. Pikuz, F. Somma, and D.W. Piston, Phys. Stat. Sol. (c) 0, No. 8 (2003) 3075.
21. A. Cricenti, R. Generosi, M. Luce, P. Perfetti, G. Margaritondo, D.B. Talley, J.S. Sanghera, I.D. Aggarwal, N.H. Tolk, Phys. Chem. Chem. Phys. 4 (2002) 2738.
22. D. de Beer, P. Stoodley, F. Roe, Z. Lewandowski, Biotechnology and Bioengineering 43 (1994) 1131.
23. J.H. van der Maas, Basic Infrared Spectroscopy, second ed., Heyden, London, 1972, 88.
24. M. Diem, S. Boydston-White, L. Chiriboga, Appl. Spectrosc. 53 (1999) 148A.
25. A. Cricenti, R. Generosi, M. Luce. P. Perfetti, G. Margoritondo, D. Talley, J. S. Sanghera, I. D. Aggarwal, N. H. Tolk, A. Congiu-Castellano, M. A. Rizzo and D. W. Piston. Biophysical J. 85 (2003) 2705.
26. W. R. Adey, Physiol. Rev. 61 (1981) 435.
27. W. R. Adey and A. F. Lawrence, in *Non linear Electrodynamics in BiologicalSystems*, edited by W. R. Adey and A. F. Lawrence (Plenum, New York, 1984).
28. Klaus Schulten, in *Festkörperprobleme*, edited by J. Treusch (Vieweg, Braunschweig, 1982), Vol. 22, pp. 61-83.
29. Christiane R. Timmel and Kevin B. Henbest, Philos. Trans. R. Soc. London, Ser. A **362**, (2004) 2573.
30. M. Hinsenkamp, A. Jercinovic, C. De Graef, F. Wilaert, and M. Heenen, Bioelectromagnetics (N.Y.) **18**, (1997) 250.
31. T. S. Tenforde, in *Handbook of Biological Effects of Electromagnetic Fields*, edited by C. Polk and E. Postow, 2nd ed. (CRC, Boca Raton, FL, 1995), pp. 185-230.
32. A. Ahlbom, N. Day, M. Feychting, E. Roman, J. Skinner, J. Dockerty, M. Linet, M. McBride, J. Michaelis, J. H. Olsen, T. Tynes, and P. K. Verkasalo, Br. J. Cancer **83** (2000) 692.
33. A. Cricenti, R. Generosi, P. Perfetti, J. M. Gilligan, N. H. Tolk, C. Coluzza, and G. Margaritondo, Appl. Phys. Lett. 73 (1998) 151.
34. P. Boukamp, R. T. Petrussevska, D. Breitkeutz, J. Hornung, A. Markham, and N. E. Fusenig, J. Cell Biol. **106**, (1988) 761.
35. S. Rieti, V. Manni, A. Lisi, D. Pozzi, L. Giuliani, A. Cricenti, R. Generosi, M. Luce, and S. Grimaldi, J. Microsc. **213** (2004) 20.
36. K. Pardali, A. Kurisaki, P. ten Dijke, D. Kardassis, and A. J. Moustakas, J. Biol. Chem. **275** (2000) 29244.
37. S. Pece and J. S. Gutkind, J. Biol. Chem. **275** (2000) 41227.